Weakening of meltwater plume reduces basal melting in summer at Ekström Ice Shelf, Antarctica

Ole Zeising[1], Tore Hattermann[2], Lars Kaleschke[1], Sophie Berger[1,*], Reinhard Drews[3], M. Reza Ershadi[3], Tanja Fromm[1], Frank Pattyn[4], Daniel Steinhage[1], and Olaf Eisen[1,5]

[1]Alfred-Wegener-Institut Helmholtz-Zentrum für Polar- und Meeresforschung, Bremerhaven, Germany
[2]Norwegian Polar Institute, Tromsø, Norway
[3]Department of Geosciences, Tübingen University, Tübingen, Germany
[4]Laboratoire de Glaciologie, Université Libre de Bruxelles, Brussels, Belgium
[5]Department of Geosciences, University of Bremen, Bremen, Germany
[*]Now at: European Commission

Correspondence: Ole Zeising (ole.zeising@awi.de)

Abstract. Basal melting of ice shelves significantly contributes to the mass loss of the Antarctic Ice Sheet. However, little is known about the ocean-driven melting of the numerous ice shelves of Dronning Maud Land in East Antarctica. We present a multi-year record of basal melt rates at the Ekström Ice Shelf, obtained using an autonomous phase-sensitive radar system. Our data reveal a low mean annual melt rate of $0.45\,\mathrm{m\,a^{-1}}$, with seasonal patterns showing reduced melt in summer and peaks
5   in winter and spring. Sea-ice growth just in front of Ekström Ice Shelf correlates with the melt rate time series. A simple ice shelf water plume simulation suggests that melting is reduced in summer in the presence of Antarctic Surface Water, which reduces the velocity of the ice shelf water plume due to the lower density contrast. In winter, when dense water from the sea ice formation erodes the stratification below the ice shelf, more vigorous plumes cause an increase in melt rates. Thus, meltwater plume velocity primarily drives the basal melt rate at the Ekström Ice Shelf, with ambient water temperature being a secondary
10 factor. Upscaling these observations to other ice shelves in this Antarctic sector will improve the overall assessment of the ice-shelf mass balance and improve future projections.

1   Introduction

The Antarctic Ice Sheet is progressively losing mass, mainly due to the ocean-driven melting of the ice shelves which restrain
15 the outflow of the grounded ice (Shepherd et al., 2018). Ice shelf thinning reduces the buttressing effect and causes the acceleration of outlet glaciers and ice streams (Dupont and Alley, 2005; Fürst et al., 2016; Reese et al., 2018). However, the East Antarctic Ice Sheet has gained mass over the last decades (Shepherd et al., 2018). Understanding the processes that contribute to basal melting is crucial to assessing the impact of a warming ocean on future ice shelf stability.

Jacobs et al. (1992) describes three modes in which ocean circulation affects basal melting. In mode 1 (cold-water cavity),
20 the sea-ice formation in winter leads to dense shelf water with temperatures at the surface freezing point that sink to the seafloor. The dense water flows along the slope of the continental shelf which often deepens toward the grounding line. The dense water

drains beneath the ice shelf and delivers heat to the ice-shelf base since the temperature of the dense shelf water exceeds the pressure-melting point of the ice-shelf base. The buoyant plume of fresh meltwater mixed with dense shelf water, called Ice Shelf Water (ISW), rises along the basal slope of the ice shelf and may fall below the freezing point when the pressure falls.

25 The super-cooled ISW may freeze on the ice-shelf base as marine ice, or it flows out of the cavity where it forms a semi-consolidated layer below the sea ice, called platelet ice (Hoppmann et al., 2020). In mode 2 (warm-water cavity), Warm Deep Water (WDW) rises above the continental shelf break and flows into the ice shelf cavity where it can cause high basal melt rates. In mode 3, warm and fresh (and hence less dense) Antarctic surface water (AASW) in summer is transported beneath the ice shelf front, leading to high basal melt rates (Hattermann et al., 2012; Lindbäck et al., 2019; Stewart et al., 2019).

30 Observing the ice–ocean interaction is challenging due to the hardly accessible ice shelf–ocean interface. Oceanographic moorings beneath or in front of ice shelves allow the observation of ocean properties that can reveal the water masses and currents and their temporal variability. Due to the logistical effort required for the deployment and the risk of destruction by passing icebergs in case of deployment in front of the shelves, these moorings are rare. However, ice shelf basal melting can be estimated over large areas by satellite remote sensing (e.g. Rignot et al., 2013; Adusumilli et al., 2020). The analysis of

35 the time-averaged melt rate pattern allows conclusions to be drawn about whether there is rather cold or warm water in the sub-ice-shelf cavity which could be linked to one of the three modes. High melt rates near the grounding line and near the ice front with low melt rates or even refreezing in between indicate a cold-water cavity with mode 1 and mode 3 melting. Such a pattern is found, among others, on the largest Antarctic ice shelves: Ross, Ronne, Filchner and Amery (Adusumilli et al., 2020). When high melt rates extend across the entire ice shelf, this indicates warm-water cavities with mode 2 melting as found

40 in the Amundsen and Bellinghausen seas in West Antarctica (Adusumilli et al., 2020).

Numerous small ice shelves exists in Dronning Maud Land (DML) in East Antarctica, whose drainage basins translate into a sea-level equivalent of over $3\,\mathrm{m}$ (Rignot et al., 2019) and whose different modes of melting contribute differently to the total mass loss. Due to relatively cold, fresh, and hence buoyant continental shelf water masses, the formation of dense High Salinity Shelf Water is limited here (Thompson et al., 2018), which is the driver of mode-1 melting in other regions of Antarctica

45 (Nicholls, 2018). Instead, Eastern Shelf Water (ESW) with temperatures close to the surface freezing point is assumed to be the dominant water mass that interacts with the DML ice shelves (Vernet et al., 2019), while seasonal downwelling of AASW beneath shallower parts of the ice shelves (Hattermann et al., 2014; Lauber et al., 2024) and intermittent inflows of WDW through topographic depressions at the continental shelf break (Lauber et al., 2023) provide additional heat for melting. Basal melt rates from satellite remote sensing revealed in general low melt rates of $0.8\pm0.3\,\mathrm{m\,a^{-1}}$ on average but higher melt rates

50 exceeding $15\,\mathrm{m\,a^{-1}}$ at the deep grounding lines of the Jelbart, Fimbul and Roi Baudouin ice shelves, where the local melting point temperature is reduced due to the higher pressure. The outflow of potentially supercooled ISW (Nøst et al., 2011), as well as the accretion of significant amounts of platelet ice beneath coastal land fast ice (Arndt et al., 2020) have also been observed. However, for most of the DML ice shelves, a detailed understanding of the year-round ice shelf cavity circulation, and the interaction of the different modes of melting is still lacking.

55 For a more detailed investigation of the ice–ocean interaction, especially with a higher temporal resolution, other methods must therefore be used. From oceanic observations, Hattermann et al. (2012) found a cold-water cavity at Fimbul Ice Shelf

with temporal inflow of modified WDW (mWDW, mode 2) and fresh surface water in summer and autumn (mode 3) that increase basal melt rates. A complementary method is given by phase-sensitive radio-echo sounding to observe the change of ice thickness of the ice shelf over a certain period and derive the basal melt rates from observations. Two studies in Dronning

60 Maud Land from Lindbäck et al. (2019) and Sun et al. (2019) used such an autonomous ground-based radar system that allows the determination of the basal melt rate with high temporal resolution. At the Nivl Ice Shelf, Lindbäck et al. (2019) found a seasonal melt pattern $4\,\mathrm{km}$ from the ice shelf front with highest melt rates of up to $5.6\,\mathrm{m\,a^{-1}}$ in summer ($0.8\,\mathrm{m\,a^{-1}}$ annual average), indicating that warm surface water was pushed in the ice shelf cavity (mode 3). At $35\,\mathrm{km}$ from the ice shelf front, no seasonality was observed, although the highest melt rate occurred in winter. Sun et al. (2019) observed the basal melt rate near

65 the grounding line of Roi Baudouin Ice Shelf and found nearly no melting in winter and highest melt rates of up to $10\,\mathrm{m\,a^{-1}}$ in summer which they linked to topographic ocean waves based on oceanic observations. Accordingly, the three ice shelves all show increased melt rates in summer, partly on the ice shelf front (Fimbul and Nivl), but also near the grounding line (Roi Baudouin), albeit due to different processes. This raises the question of temporal melt rate variability and the responsible processes at other ice shelves in DML.

70   In this study, we investigate the ice–ocean interaction at the Ekström Ice Shelf based on observations of basal melt rates from a 4-year-long time series with an autonomous phase-sensitive radar and a time series of sea-ice growth in front of the Ekström Ice Shelf. To further study the relation between sea-ice growth and melt rate, we used an idealized plume model to gain further insights into the processes leading to the observed seasonality of basal melting.

2   Study area

75 The Ekström Ice Shelf is located in the western Dronning Maud Land, East Antarctica, and covers an area of $\sim 6800\,\mathrm{km^2}$ (Neckel et al., 2012). The two ice rises Søråsen and Halvfarryggen confine the Ekström Ice Shelf and partly separate it from the two smaller ice shelves Quar and Atka (Fig. 1). The ice thickness varies from $1000\,\mathrm{m}$ at the grounding line to $250\,\mathrm{m}$ at the calving front, where the ice velocity is roughly $220\,\mathrm{m\,a^{-1}}$ (Mouginot et al., 2019a, b; Morlighem et al., 2020; Morlighem, 2020). The bathymetry below the ice shelf consists of an inland-sloping trough that reaches a maximum depth of $1100\,\mathrm{m}$ below

80 sea level near the grounding line (Eisermann et al., 2020; Smith et al., 2020). The minimum seafloor depth of $320\,\mathrm{m}$ is located on the continental shelf break which is sufficiently shallow to prevent the inflow of WDW that circulates along the shelf break into the cavity below Ekström Ice Shelf (Eisermann et al., 2020). The water column thickness in the cavity below the Ekström Ice Shelf ranges from $220\,\mathrm{m}$ at the front to $> 400\,\mathrm{m}$ for larger parts in the centre of the trough (Eisermann et al., 2020; Smith et al., 2020). Observations from sub-ice-shelf conductivity temperature depth (CTD) profiles showed that most of the cavity

85 below Ekström Ice Shelf is filled with relatively cold ESW (in situ temperatures of $-1.9\,°\mathrm{C}$, practical salinity of 34.4), while a buoyant plume of ISW (colder, less saline) is present near the ice-shelf base (Smith et al., 2020). The Warm Deep Water that is suppressed below the continental shelf break in this region, is not expected to enter below the ice shelf (Smith et al., 2020). However, observations in front of the ice shelf (Nøst et al., 2011) and below the neighbouring Fimbulisen Ice Shelf (Hattermann et al., 2012; Lauber et al., 2024) indicate that remnants of fresher, solar-heated AASW may enter several hundred
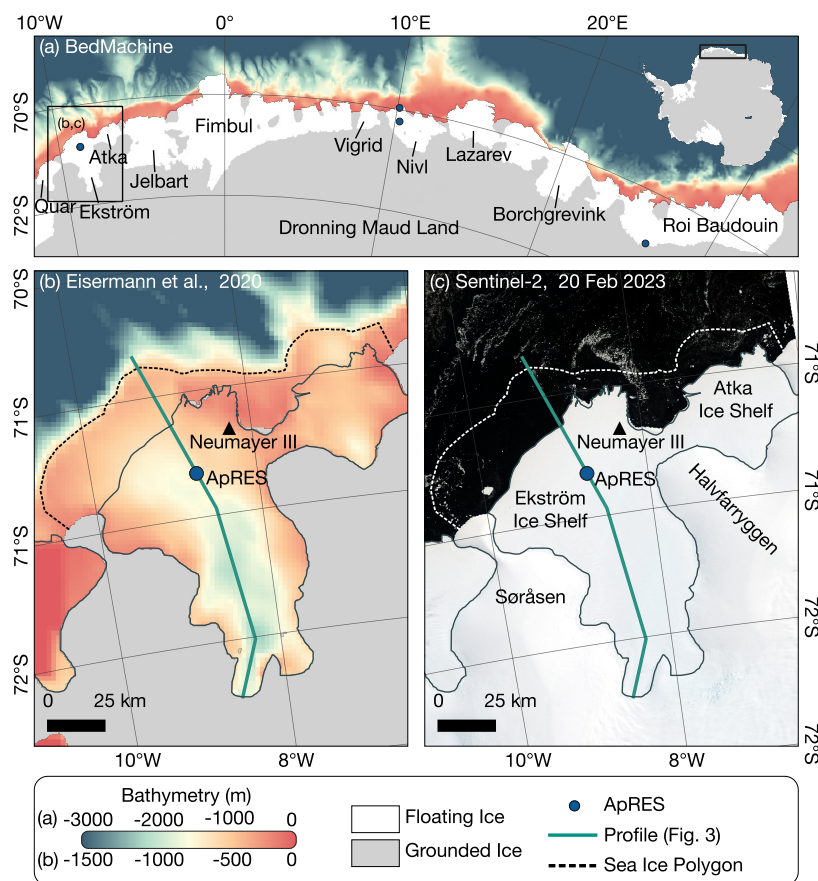
Figure 1. (a) Overview of Dronning Maud Land's ice shelves with the bathymetry in front of ice shelves from BedMachine (Morlighem et al., 2020; Morlighem, 2020). The blue dots show the location of the ApRES measurements at Ekström Ice Shelf (this study), Nivl Ice Shelf (Lindbäck et al., 2019) and Roi Baudouin Ice Shelf (Sun et al., 2019). (b) Bathymetry below and in front of Ekström Ice Shelf from Eisermann et al. (2020). The black triangle marks the location of the German station Neumayer III. The green line represents the location of the profile shown in Fig. 4. The dashed line marks the polygon within which the sea-ice growth has been estimated. (c) Copernicus Sentinel-2 image from 20 February 2023, retrieved from the Copernicus SciHub on 31 July 2023.

meters below the ice shelves along the DML coast. Estimated basal melt rates of the Ekström Ice Shelf from satellite remote sensing methods are relatively low. Adusumilli et al. (2020) found an average basal melt rate of $1.0 \pm 1.2 \, \mathrm{m \, a^{-1}}$ (period 1994 – 2018) over the entire ice shelf and a maximum melt rate exceeding $3 \, \mathrm{m \, a^{-1}}$ near the grounding line as well as near the German station Neumayer III. Slightly lower melt rates of $< 1.1 \, \mathrm{m \, a^{-1}}$ were found by Neckel et al. (2012) for the period between 1996 and 2006.

3 Data and methods

3.1 Basal melt rates

To measure basal melt rates, we operated an autonomous phase-sensitive radio-echo sounder (ApRES, Brennan et al., 2014; Nicholls et al., 2015) on the Ekström Ice Shelf $25\,\mathrm{km}$ upstream of the ice shelf front (Fig. 1; location at 70.82 °S, 8.73 °W on 02 April 2020 termed MIMO-EIS-8). An ApRES is a ground-penetrating frequency-modulated continuous-wave (FMCW) radar that transmits chirps throughout $1\,\mathrm{s}$ while it increases the frequency of the electromagnetic wave from 200 to $400\,\mathrm{MHz}$. The received signal is mixed with a replica of the transmitted signal to obtain a de-ramped signal that is sampled with $40\,\mathrm{kHz}$ (Nicholls et al., 2015).

The ApRES and two skeleton slot antennas were placed below the surface for protection from wind and snowdrifts. It performed hourly measurements consisting of 20 chirps between April 2020 and November 2023. Short gaps of two to three days exist in the recorded time series (09–10 January 2021, 25–26 November 2021, 31 December 2022 – 02 January 2023), at which the device was dismounted and used for other measurements, and a longer gap from 1 April to 16 May 2021.

The signal processing we applied to the raw data follows the previous work by Brennan et al. (2014), Nicholls et al. (2015) and Stewart et al. (2019). First, we rejected the first chirp of each measurement and stacked the remaining chirps to get a better signal-to-noise ratio. Next, to obtain an amplitude and phase profile from the stacked de-ramped signal, we applied a spectral analysis. For further processing, an unambiguously determined range from the phase is necessary, which is achieved when the phase variation over a range bin is $< 2\pi$. Thus, we artificially increased the resolution using a zero-padding method with a pad-factor of 8 before the spectral analysis (Brennan et al., 2014). The outcome of the spectral analysis is an amplitude and a phase profile as a function of two-way travel time. Finally, we obtained a range profile by converting the two-way travel time into a range using a propagation velocity of $168\,914\,\mathrm{km\,s^{-1}}$ according to the ordinary relative permittivity of 3.15. The range resolution is $0.053\,\mathrm{m}$, while the resolution of the phase is about $1°$, corresponding to $1\,\mathrm{mm}$ in range.

The determination of the basal melt rate from an ApRES time series is based on the analysis of the ice thickness change and the decomposing of the processes contributing to it (Nicholls et al., 2015). Thus, the change in ice thickness ΔH within the time interval Δt is the sum of the thickness changes caused by firn compaction ΔH_f, vertical strain ΔH_ε and basal melting ΔH_b:

$$\frac{\Delta H}{\Delta t} = \frac{\Delta H_f}{\Delta t} + \frac{\Delta H_\varepsilon}{\Delta t} + \frac{\Delta H_b}{\Delta t}. \tag{1}$$

Since the ApRES was located below the surface, the measured ice thickness was not affected by snow accumulation. Solving Equation (1) for the melt rate a_b gives:

$$a_b = -\frac{\Delta H_b}{\Delta t} = -\left(\frac{\Delta H}{\Delta t} - \frac{\Delta H_f}{\Delta t} - \frac{\Delta H_\varepsilon}{\Delta t} \right), \tag{2}$$

where positive a_b represents basal melting.

For the melt-rate analysis, we follow the method described by Zeising and Humbert (2021) and Humbert et al. (2022), which are based on the previous work by Nicholls et al. (2015) and Stewart et al. (2019). The ApRES time series allows the

high-precision determination of ΔH, ΔH_f, and ΔH_ε with millimetre accuracy. To this end, we divided the range profile into $6\,\mathrm{m}$ long segments with $3\,\mathrm{m}$ overlap below a depth of $10\,\mathrm{m}$. Around the basal reflection, identified by a strong increase in amplitude, we used a larger segment of $10\,\mathrm{m}$ size ($-9\,\mathrm{m}$ to $+1\,\mathrm{m}$ with respect to the basal reflection). For the basal segment,

130 we derived displacements from complex-valued cross-correlation of the phase of all pairwise time-consecutive measurements. For the internal segments, we calculated the complex cross-correlation of the first measurement (t_1) with the same segment of each repeated measurement (t_i). We used the lag of the highest amplitude correlation coefficient to find the correct phase-shift minimum, the sum of which gives the vertical displacement.

The change in ice thickness and the processes contributing to it can now be determined based on the vertical displacements.

135 The cumulative change in ice thickness results from the time series of the displacement of the basal segment. The contributions of firn compaction and vertical strain must be calculated based on the vertical displacement u_z of various englacial segments. The vertical strain ε_{zz} is defined as the vertical derivative of the vertical displacement u_z:

$$\varepsilon_{zz} = \frac{\partial u_z}{\partial z}. \tag{3}$$

We calculated the derivative of the vertical displacements based on a linear regression analysis assuming constant strain over

140 depth as expected for the shallow-shelf flow regime of ice shelves. Here, we considered only those segments below the range of $100\,\mathrm{m}$ and $20\,\mathrm{m}$ above the basal return to avoid firn compaction and the basal return to influence the strain rate analysis. The linear regression analysis gives the cumulative displacement

$$u_z(z) = \varepsilon_{zz} z + \Delta H_f, \tag{4}$$

where the firn compaction ΔH_f is the intercept at the surface. The strain contribution to the change in ice thickness ΔH_ε is

145 then the integral over the ice thickness H:

$$\Delta H_\varepsilon = \int_0^H \varepsilon_{zz} \, \mathrm{d}z. \tag{5}$$

Appendix A shows the analysis of the basal melt rate for one example from 2020.

During the three interruptions in the ApRES time series in January 2021, November 2021, and December 2022/January 2023, the ApRES was locally repositioned, a few metres laterally away from the previous location and placed again close to

150 the surface to avoid burial over time. Therefore, we redefined t_1 as the first measurement after these interruptions. To determine the melt rate at a certain point in time, we smoothed the data by applying a $36\,\mathrm{h}$ moving average filter, and calculated the basal melt rates based on the gradient in a $7\,\mathrm{d}$ moving window. To represent the variability of the melt rate on sub-weekly time scales, we also calculated the $7\,\mathrm{d}$ standard deviation of the basal melt rates based on the gradient in a $1\,\mathrm{d}$ moving window. The uncertainty of the basal melt rate is based on the uncertainty of the strain estimation and the determination of the ice thickness

155 change. On average the uncertainty of the basal melt rate amounts to $0.02\,\mathrm{m\,a^{-1}}$.

3.2 Sea-ice growth

To further investigate the relation between sea-ice formation and an increase in melt rate, we determined sea-ice growth over the continental shelf in front of the Ekström and Atka ice shelves (Fig. 1b, c). Sea-ice growth was estimated using the simple model of Pease (1987), which relates the sea-ice growth to the heat loss at the ice-free ocean surface in a polynya. We used
160   surface wind speed and air temperature from JRA-55 reanalysis (Kobayashi et al., 2015) to calculate heat loss over the ice-free ocean. The open water area was derived from AMSR-2 passive microwave data twice daily on a $3.125\,\mathrm{km}$ grid (Beitsch et al., 2014). Time series of sea-ice growth were derived within a fixed polygon area (Fig. 1c) for the same period as the ApRES measurements.

3.3 Plume model

165   To investigate the impact of varying ocean properties on basal melt rates beneath the Ekström Ice Shelf, we employed the idealised ice-shelf plume model of Jenkins (1991), which has previously been used to describe the larger-scale circulation beneath ice shelves. Assuming that circulation and mixing beneath the ice shelf are primarily driven by thermohaline processes, the model describes a buoyant meltwater-laden plume that rises along the sloping ice base. The plume grows through the entrainment of ambient ocean waters, and the heat brought into the plume, as a result, drives melting at the ice–ocean interface.
170   Omitting Coriolis' effect, the system is parameterised along a one-dimensional flowline, described by four ordinary differential equations with prognostic variables for the plume thickness D, speed U, temperature T, and salinity S. The model is steady in time, uniform in the across-flow direction, and depth-integrated, leaving the along-track distance X as the only independent variable (Jenkins, 2011).

Given the confined configuration of the Ekström Ice Shelf along a quasi-one-dimensional flowline geometry, we assume that
175   the idealised model captures the basic features of the cavity circulation of this ice shelf, while tides superimpose to further modulate the melt rates. The plume dynamics are then largely governed by the slope of the ice base and the density difference between the plume and the ambient ocean properties. The former is prescribed based on BedMachine (Fig. 4a; Morlighem et al., 2020; Morlighem, 2020), which includes a seismic profile running from the grounding line to the ice front of the Ekström Ice Shelf (Smith et al., 2020). We performed two simulations with different vertical profiles of ambient temperature and salinity to
180   investigate the impact of seasonally varying water mass properties on the cavity circulation and melt rates. In winter, convection after sea-ice formation produces a well-mixed body of Winter Water that occupies the continental shelf (Nøst et al., 2011). We mimic these conditions with profiles of temperature and salinity that resemble the observed ESW properties inside the cavity (Smith et al., 2020), with a slight linear increase from $-1.88\,^{\circ}\mathrm{C}$ to $-1.8\,^{\circ}\mathrm{C}$ and from 34.30 to 34.34 of the in situ temperature and practical salinity from the surface to $900\,\mathrm{m}$ depth, assuring the stability of the water column. For summer conditions, we
185   adjust the linear profiles to mimic the presence of stratified AASW inside the cavity, by increasing the surface temperature to $-1.7\,^{\circ}\mathrm{C}$ and decreasing the surface salinity to 33.80, to values which are representative of AASW end-member properties that have been observed in the open ocean (Nøst et al., 2011) and below the neighbouring Fimbulisen Ice Shelf (Hattermann et al.,

7

2012). The potential density–depth profiles show that both profiles converge to the same ESW properties at depth, but with an enhanced stratification inside the cavity during the summer case.

4 Results

4.1 Basal melt rate

The time series from 2020 to 2023 reveals a low melt rate averaging $0.45 \pm 0.30 \, \mathrm{m \, a^{-1}}$ (mean $\pm$ standard deviation) with a seasonal melt pattern (Tab. 1, Fig. 2). Basal melt rates are reduced to a minimum of $0.25 \pm 0.14 \, \mathrm{m \, a^{-1}}$ in summer (December, January, February; DJF; 2020–2023 average), they increase slightly to $\sim 0.4 \, \mathrm{m \, a^{-1}}$ in autumn (March, April, May; MAM) and during winter (June, July, August; JJA), and reach their maximum in spring (September, October, November; SON) with an average of $0.70 \pm 0.38 \, \mathrm{m \, a^{-1}}$ (Tab. 1, Fig. 2). From July/August until October/November, melt events occur that last two to four weeks. At the beginning of these melt events, the melt rate increased abruptly to $\sim 1 \, \mathrm{m \, a^{-1}}$ and more. The strongest melt event occurred in September 2020, when the melt rate increased from 0.21 to $1.81 \, \mathrm{m \, a^{-1}}$ (7-day average). After two weeks, the melt rate decreased again to $0.54 \, \mathrm{m \, a^{-1}}$, before the next melt event occurred.

The seasonality was strongest in 2020 with on average 5 times higher melt rates in spring than in summer 2020/21 (Tab. 1). In 2021 and 2022, we see a weaker seasonality with only 2 times higher melt rates in spring compared to summer. The trend of weaker seasonality from 2020 and 2022 is caused by lower melt rates in spring that decreased from $1.08 \pm 0.31 \, \mathrm{m \, a^{-1}}$ in 2020 to $0.52 \pm 0.31 \, \mathrm{m \, a^{-1}}$ in 2022.

Table 1. Mean value and standard deviation of basal melt rate separated for austral autumn (MAM), winter (JJA), spring (SON), and summer (DJF). The annual mean represents the March–February average value.

Basal melt rate $(\mathrm{m \, a^{-1}})$

Year	2020/21*	2021/22	2022/23	2023/24**	Average
Autumn	0.25 ± 0.08	0.34 ± 0.08	0.47 ± 0.12	0.40 ± 0.14	0.38 ± 0.13
Winter	0.32 ± 0.19	0.53 ± 0.36	0.46 ± 0.15	0.37 ± 0.21	0.42 ± 0.25
Spring	1.08 ± 0.31	0.59 ± 0.30	0.52 ± 0.31	0.55 ± 0.25	0.70 ± 0.38
Summer	0.23 ± 0.13	0.27 ± 0.16	0.24 ± 0.13	–	0.25 ± 0.14
Annual	0.50 ± 0.42*	0.43 ± 0.28	0.42 ± 0.22	0.43 ± 0.22**	0.45 ± 0.30

*In 2020/21, the measurements cover only the months of April 2020 to February 2021.

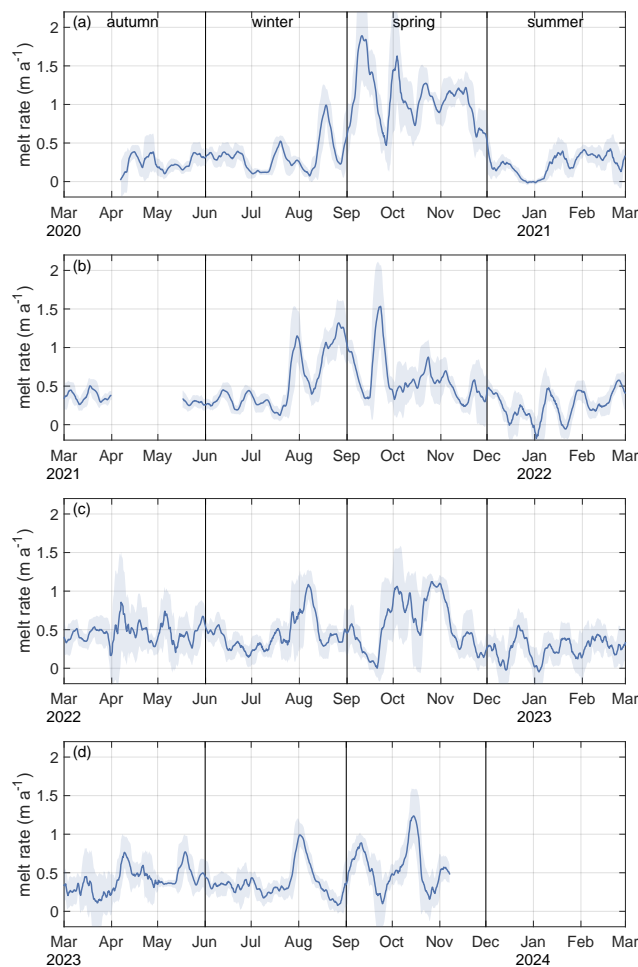**In 2023/24, the measurements cover only the months of March 2023 to October 2023.

8

Figure 2. Time series of 7-day average basal melt rate from autumn 2020 to spring 2023 (blue line) with sub-weekly variability represented by the standard deviation (shaded area).

4.2 Sea-ice growth

205 A comparison of the melt rate and sea-ice growth time series with their average values for the individual seasons shows a similar pattern (Figs. 3, B1). Sea-ice growth and melt rates have a minimum in summer, followed by an increase in autumn and winter and a maximum in spring. Only in the spring of 2023 was the sea-ice growth lower than in the autumn and winter of the same year. Despite the reduced sea-ice growth for spring, the melt rate appears to have continued to increase. Since the basal melt rate time series ended at the beginning of November and thus the observation does not cover the whole period, this value

210 should be interpreted with caution.

Similar to the melt rate time series, the high-resolution time series of the sea-ice growth (Fig. B1) shows events of higher sea-ice growth with a comparable duration to the observed basal-melt events. Although some of the melt events can be connected
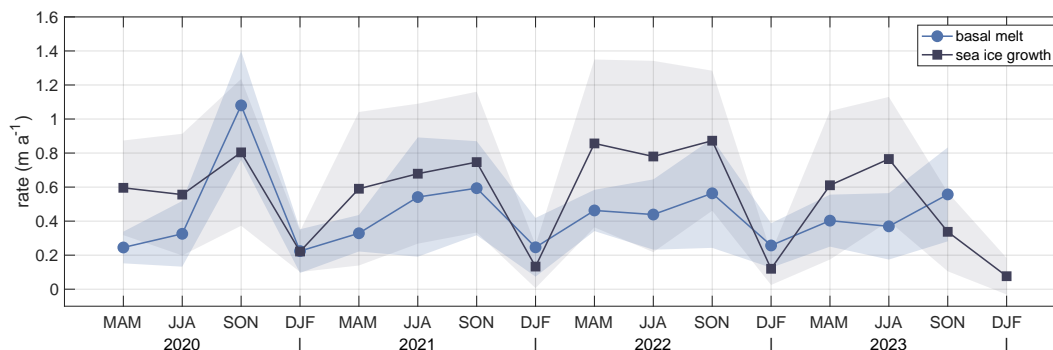
Figure 3. Three-month averages of sea-ice growth (black line) above continental shelf (dashed line in Figs. 1b,c) and basal melt rate from ApRES location (blue line) separated for austral autumn (March, April, May; MAM), winter (June, July, August; JJA), spring (September, October, November; SON), and summer (December, January, February; DJF) from 2020 to 2023. The markers show the mean rate for autumn/winter/spring/summer and the shaded areas show the standard deviation. In autumn 2020, the melt rate time series only covers the months of April and May and in spring 2023 only the months of September to early November. The non-average sea-ice growth is shown in B1.

to a previous increase in sea-ice growth, other events in sea-ice growth occurred in autumn without an increase in the melt rate being measured. Additionally, there is no apparent agreement in 2022 and 2023 between the sea-ice growth and the melt rate

215 (Fig. B1c, d). Generally, the time scale of this variability resembles the fortnightly spring-neap cycle, on which tidal currents strengthen and weaken in Atka-bay (Smith et al., 2009). It is easy to imagine that the varying intensity of the tides modulate the efficiency of the sea ice formation in coastal polynyas, as well as the exchange of water masses on the continental shelf with the ice shelf cavity, explaining the characteristic time scale of the observed variability.

4.3 Plume model

220 The simulation results show no significant differences in the plume temperature, but differences in the plume velocity (Fig. 4). In the winter simulation, the plume velocity is on average $0.06\,\mathrm{m\,s}^{-1}$ (or 165%) above that of the summer simulation. The increased flow velocity of the ISW plume enhances the turbulent heat exchange at the ice–ocean interface, resulting in an increased melt rate of an average of $1.4\,\mathrm{m\,a}^{-1}$. The difference in melt rate is largest between 15 and $30\,\mathrm{km}$ from the grounding line where the simulated melt rate is 3 to $5\,\mathrm{m\,a}^{-1}$ above the summer melt rate. At the ApRES location, the increase in melt rate

225 is still $0.5\,\mathrm{m\,a}^{-1}$ and thus of similar size to our observations.

5 Discussion

The results of the simulation allow the following interpretation for summer and winter conditions: In summer, the low-density contrast between the rising ISW and the AASW that is pushed below the ice shelf weakens the meltwater plume by reducing its velocity, or even lead to the detachment of the plume from the ice base. Because the meltwater plume velocity is reduced and
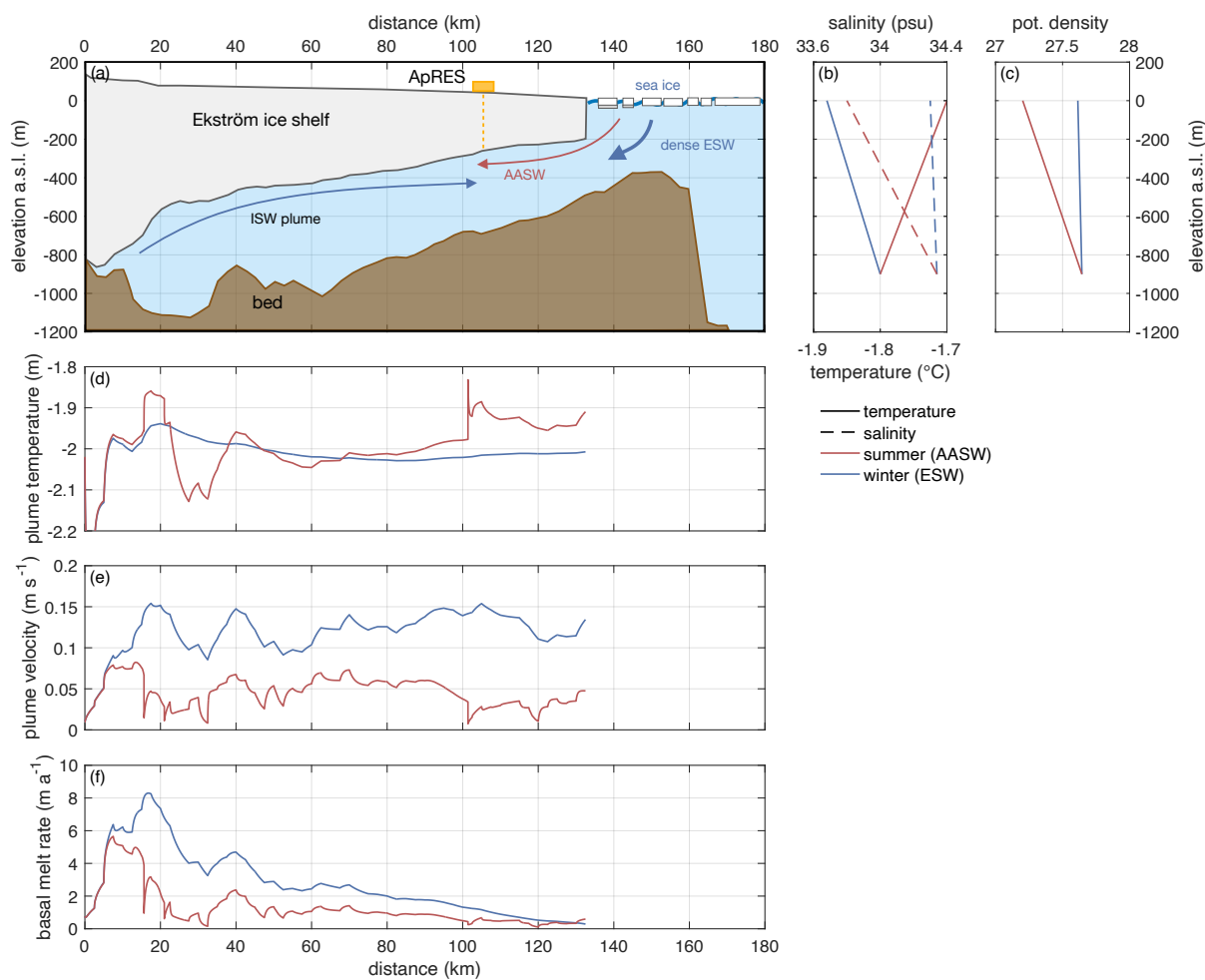
Figure 4. Simulation of ISW-plume in the cavity of Ekström ice shelf. (a) Sketch of ice shelf geometry (Morlighem et al., 2020; Morlighem, 2020), bathymetry (Smith et al., 2020) and ocean currents for ISW plume, AASW in summer and ESW in winter. The location of this transect is shown in Figure 1b,c. (b) Salinity–depth (dashed lines) and temperature–depth (solid line) profiles, and (c) potential density–depth profiles for summer (AASW) and winter (ESW) conditions. (d) Plume temperature and (e) velocity, as well as (g) basal melt rate for summer and winter conditions in the cavity.

230   the additional heat provided by AASW is small at the ApRES site, melt rates are low in summer. In winter, sea-ice formation in front of the Ekström Ice Shelf erodes the stratification on the continental shelf and replaces the AASW inside the cavity with a homogeneous body of ESW. The higher density contrast between the ambient ESW and the rising plume is sufficient to drive turbulence at the ice–ocean interface. This increases the heat flux into the ice and thus enhances basal melting. When the plume rises further, the pressure decreases and the temperature of the plume can fall below the freezing point. The super-cooled ISW

235 plume is deposited as platelet ice beneath the sea ice in front of the ice shelf. This agrees with the results of Arndt et al. (2020), who found seasonality in platelet ice formation at Atka Bay with the highest accumulation rates in winter and spring.

The interpretation of the simulation suggests that the melt rate time series shows a reduced melt rate in summer while the reactivation of the plume restores normality. Thus, this process differs from mode 1 described in Jacobs et al. (1992). Mode 1 assumes that sea-ice formation enhances basal melting through thermal effects, supplying dense High Salinity Shelf Water

240 with temperatures at the surface freezing point to the deeper parts of the Filchner-Ronne, Ross and Amery ice shelf cavities, which are normally filled by even colder ISW. In the case of Ekström Ice Shelf, we assume that most of the cavity is filled with water close to the surface freezing point (Smith et al., 2020), such that the thermal effect of sea ice melt water is small (and with no evidence for High Salinity Shelf Water formation in this sector of Antarctica (Thompson et al., 2018)). Instead, the simulations show that the density contrast between the rising ISW and the ambient water in the cavity modulates the plume

245 velocity and thus the basal melt rate, by affecting the turbulent heat transfer at the ice–ocean interface. In this regime, the temperature of the ambient water is only secondary to the increase or decrease in melt rate, while this highlights the role of the sea-ice formation in the reactivation of the plume. We draw the conclusion that a reduced sea-ice formation in front of the ice shelf, such as widely observed in Antarctica in 2023, as well as a freshening of upper ocean properties, could result in a reduced mean annual melt rate. Hence, the effect of sea-ice formation and ice shelf cavity stratification will need to be taken

250 into account together with other processes like potential warming of the AASW (Kusahara and Hasumi, 2013; Kusahara et al., 2023) and changes in coastal winds (Dinniman et al., 2015) that also influence the basal melt rate at Ekström Ice Shelf.

The seasonality of the melt rate and its sensitivity to the stratification inside the cavity at the Ekström Ice Shelf differs from from processes that have been observed at ice shelves in DML. At Nivl ice shelf, Lindbäck et al. (2019) found that higher melt rates of up to $5.6\,\mathrm{m\,a^{-1}}$ appear when warm fresh AASW is pushed below the ice shelf by winds. However, at greater distances

255 from the ice front, Lindbäck et al. (2019) found no pronounced seasonality and lower melt rates of below $2.0\,\mathrm{m\,a^{-1}}$ despite of one melt event in winter. The Ekström Ice Shelf has an ice thickness of $\sim 250\,\mathrm{m}$ at the calving front, the Nivl Ice Shelf is about $90\,\mathrm{m}$ thinner. The lower ice thickness allows warmer AASW to be pushed under the Nivl Ice Shelf and therefore increases melt rates in summer near the calving front due to the additional heat (Lindbäck et al., 2019). While a similar effect might dominate the meltrate seasonality closer to the calving front of Ekström Ice Shelf, its more confined geometry and deeper grounding

260 line promotes the development of coherent ISW plumes which modulate basal melting when interacting with the seasonally varying cavity stratification. The absence of seasonality further away from the ice shelf front in conjunction with the low melt rate of $< 1\,\mathrm{m\,a^{-1}}$ at Nivl Ice Shelf is consistent with less pronounced plume-driven melting throughout the year.

The existing melt rate measurements in DML as well as the plume simulation show that the melt rate as well as the intensity and type of seasonality can strongly depend on the relative position on the ice shelf. Further measurements are needed to better

265 understand the spatial and temporal variation of the basal melt rate. In addition, ocean simulations indicate that an increase in melt rates of the eastern Weddell Sea ice shelves can trigger a melt regime change of Filchner-Ronne Ice Shelf ($14\,\mathrm{m}$ sea-level equivalent (Rignot et al., 2019)) towards significant higher melt rates (Hoffman et al., 2024). For this reason, melt rates in DML and of other ice shelves in the Weddell Sea should be further monitored using a network of ApRES.

6 Conclusions

270 In this study, we investigated the ice–ocean interaction at the Ekström Ice Shelf using a combination of basal melt rate observations from a 4-year-long ApRES time series, a time series of sea-ice growth and a ice shelf plume simulation. Our analysis provides valuable insights into the seasonality of basal melting, contributing to a deeper understanding of the processes driving ice shelf basal melting in East Antarctica. The observed basal melt rates at the Ekström Ice Shelf were found to be relatively low, averaging $0.45\,\mathrm{m\,a^{-1}}$, with a distinct seasonal pattern. The melt rates were lowest during the summer and highest in

275 the spring, with a few weeks long melt events occurring predominantly from late winter to early spring. The sea-ice growth revealed a similar seasonal pattern that highlights the impact of sea-ice formation on the ocean conditions in the ice-shelf cavity. Simulations with a meltwater plume model suggests that the seasonal inflow of Antarctica surface water enhances the stratification inside the cavity and weakens the plume. Due to low contrast in density, the velocity of the ice shelf water plume reduces and, as a result, the melt rates decrease. In winter, the plume is reactivated due to dense water from the sea-ice forma-

280 tion that erodes the stratification and increases the density contrast. We conclude that the melt rate is primarily affected by the plume velocity, while the temperature of the ambient water is only secondary. Thus, lower sea-ice growth in the future could result in a reduced mean annual melt rate. Overall, our study underscores the importance of continuous and high-resolution observations to capture the temporal variability of basal melt processes. The findings emphasise the need for further research to analyse the processes under the entire ice shelf as well as of other ice shelves of the Dronning Maud Land to correlate melt rate

285 trends with a climate signal. In addition, the use of models that can capture complex processes is needed, as well as oceanic measurements to validate model results. By enhancing our understanding of these ice–ocean interaction, we can better assess the future contributions of Antarctic ice shelves to global sea-level rise.

Data availability. Raw data and the time-series of basal melt rates are submitted to the World Data Center PANGAEA

Appendix A: ApRES analysis

Table A1. Derived quantities from ApRES measurements (03 April 2020 – 31 December 2020; Fig. A1) used for basal melt rate determination: Ice thickness change (ΔH), thickness change due to firn compaction (ΔH_f), due to vertical strain (ΔH_ε), the vertical strain itself ($\dot\varepsilon_{zz}$) and the basal melt rate (a_b). Negative values contribute to the thinning of the ice column, whereas a positive melt rate represents melting.

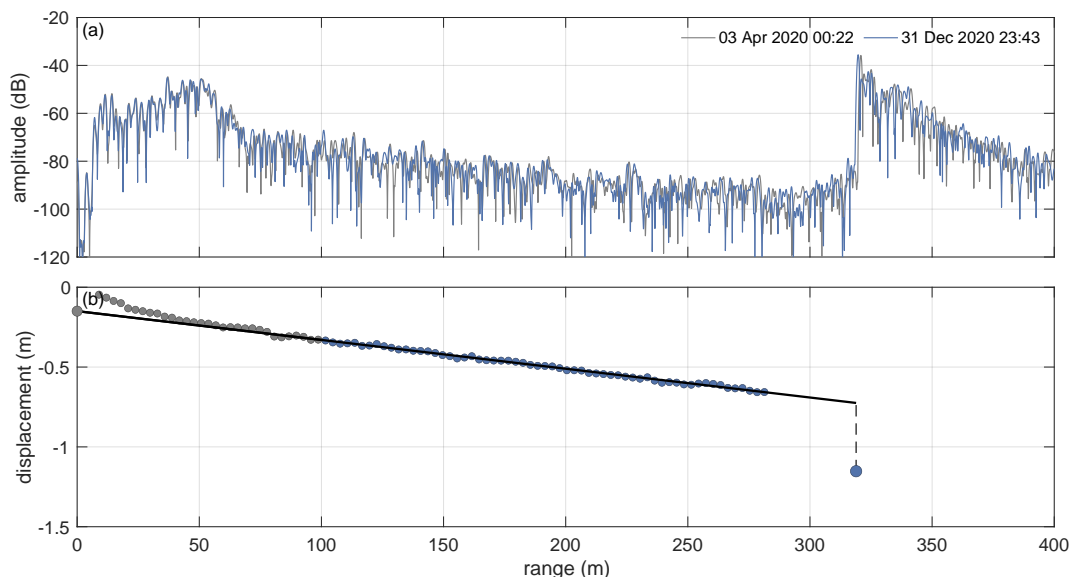| Year	$\Delta H\,(\mathrm{m\,a^{-1}})$	$\Delta H_f\,(\mathrm{m\,a^{-1}})$	$\dot\varepsilon_{zz}\,(\mathrm{a^{-1}})$	$\Delta H_\varepsilon\,(\mathrm{m\,a^{-1}})$	$a_b\,(\mathrm{m\,a^{-1}})$
2020	-1.54 ± 0.01	-0.20 ± 0.01	-0.0024 ± 0.0001	-0.77 ± 0.01	0.57 ± 0.01

13

Figure A1. Basal melt rate analysis of ApRES data from 2020. (a) Amplitude profiles of the first (grey line) and last measurement (blue line) in 2020. (b) Vertical displacement of the basal segment (large blue dot) and of internal segments (small dots). Those internal segments used for strain rate analysis (gradient of solid black line) are coloured in blue. The dashed line represents the displacement caused by basal melting.

Appendix B: Sea-ice growth

Table B1. Mean value and standard deviation of sea-ice growth separated for austral autumn (March, April, May), winter (June, July, August), spring (September, October, November), and summer (December, January, February). The mean annual represents the March–February mean value.

Sea-ice growth $(\mathrm{m\,a^{-1}})$

Year	2020/21	2021/22	2022/23	2023/24	Average
Autumn	0.60 ± 0.28	0.59 ± 0.45	0.86 ± 0.49	0.61 ± 0.44	0.66 ± 0.43
Winter	0.56 ± 0.36	0.68 ± 0.41	0.78 ± 0.56	0.77 ± 0.36	0.69 ± 0.44
Spring	0.80 ± 0.43	0.75 ± 0.41	0.87 ± 0.41	0.34 ± 0.23	0.69 ± 0.43
Summer	0.22 ± 0.12	0.13 ± 0.13	0.12 ± 0.10	0.08 ± 0.11	0.14 ± 0.13
Annual	0.55 ± 0.38	0.54 ± 0.44	0.67 ± 0.53	0.48 ± 0.41	0.56 ± 0.45
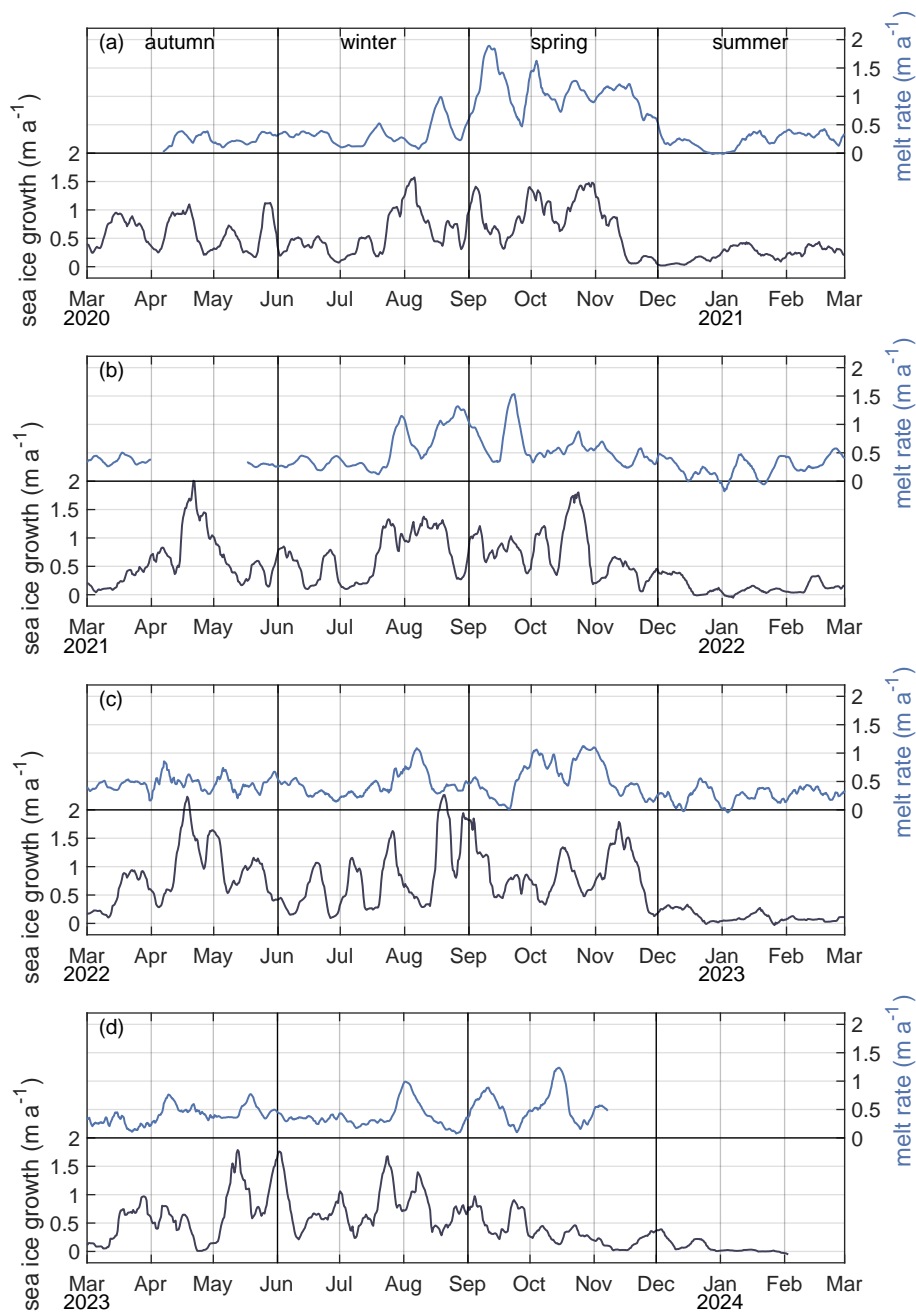
Figure B1. Average sea-ice growth (black line) above continental shelf (Fig. 1b, c) and basal melt rate (blue line) from 2020/21 to 2023/24.

References

Adusumilli, S., Fricker, H. A., Medley, B., Padman, L., and Siegfried, M. R.: Interannual variations in meltwater input to the Southern Ocean
    from Antarctic ice shelves, Nature Geoscience, 13, 616–620, https://doi.org/10.1038/s41561-020-0616-z, 2020.

Alfred-Wegener-Institut Helmholtz-Zentrum für Polar- und Meeresforschung: Neumayer III and Kohnen Station in Antarctica operated by
    the Alfred Wegener Institute, Journal of large-scale research facilities, 2, https://doi.org/10.17815/jlsrf-2-152, 2016.

Arndt, S., Hoppmann, M., Schmithüsen, H., Fraser, A. D., and Nicolaus, M.: Seasonal and interannual variability of landfast sea ice in Atka
    Bay, Weddell Sea, Antarctica, The Cryosphere, 14, 2775–2793, https://doi.org/10.5194/tc-14-2775-2020, 2020.

Beitsch, A., Kaleschke, L., and Kern, S.: Investigating High-Resolution AMSR2 Sea Ice Concentrations during the February 2013 Fracture
    Event in the Beaufort Sea, Remote Sensing, 6, 3841–3856, https://doi.org/10.3390/rs6053841, 2014.

Brennan, P. V., Lok, L. B., Nicholls, K., and Corr, H.: Phase-sensitive FMCW radar system for high-precision Antarctic ice shelf profile
    monitoring, IET Radar, Sonar & Navigation, 8, 776–786, https://doi.org/10.1049/iet-rsn.2013.0053, 2014.

Dinniman, M. S., Klinck, J. M., Bai, L.-S., Bromwich, D. H., Hines, K. M., and Holland, D. M.: The Effect of Atmospheric Forcing Resolu-
    tion on Delivery of Ocean Heat to the Antarctic Floating Ice Shelves, Journal of Climate, 28, 6067 – 6085, https://doi.org/10.1175/JCLI-
    D-14-00374.1, 2015.

Dupont, T. K. and Alley, R. B.: Assessment of the importance of ice-shelf buttressing to ice-sheet flow, Geophysical Research Letters, 32,
    https://doi.org/10.1029/2004GL022024, 2005.

Eisermann, H., Eagles, G., Ruppel, A., Smith, E. C., and Jokat, W.: Bathymetry Beneath Ice Shelves of Western Dronning
    Maud Land, East Antarctica, and Implications on Ice Shelf Stability, Geophysical Research Letters, 47, e2019GL086 724,
    https://doi.org/10.1029/2019GL086724, 2020.

Fürst, J. J., Durand, G., Gillet-Chaulet, F., Tavard, L., Rankl, M., Braun, M., and Gagliardini, O.: The safety band of Antarctic ice shelves,
    Nature Climate Change, 6, 479, https://doi.org/10.1038/nclimate2912, 2016.

Hattermann, T., Nøst, O. A., Lilly, J. M., and Smedsrud, L. H.: Two years of oceanic observations below the Fimbul Ice Shelf, Antarctica,
    Geophysical Research Letters, 39, https://doi.org/10.1029/2012GL051012, 2012.

Hattermann, T., Smedsrud, L., Nøst, O., Lilly, J., and Galton-Fenzi, B.: Eddy-resolving simulations of the Fimbul Ice Shelf cavity circulation:
    Basal melting and exchange with open ocean, Ocean Modelling, 82, 28–44, https://doi.org/10.1016/j.ocemod.2014.07.004, 2014.

Hoffman, M. J., Branecky Begeman, C., Asay-Davis, X. S., Comeau, D., Barthel, A., Price, S. F., and Wolfe, J. D.: Ice-shelf freshwa-
    ter triggers for the Filchner–Ronne Ice Shelf melt tipping point in a global ocean–sea-ice model, The Cryosphere, 18, 2917–2937,
    https://doi.org/10.5194/tc-18-2917-2024, 2024.

Hoppmann, M., Richter, M. E., Smith, I. J., Jendersie, S., Langhorne, P. J., Thomas, D. N., and Dieckmann, G. S.: Platelet ice, the Southern
    Ocean's hidden ice: a review, Annals of Glaciology, 61, 341–368, https://doi.org/10.1017/aog.2020.54, 2020.

Humbert, A., Christmann, J., Corr, H. F. J., Helm, V., Höyns, L.-S., Hofstede, C., Müller, R., Neckel, N., Nicholls, K. W., Schultz, T.,
    Steinhage, D., Wolovick, M., and Zeising, O.: On the evolution of an ice shelf melt channel at the base of Filchner Ice Shelf, from
    observations and viscoelastic modeling, The Cryosphere, 16, 4107–4139, https://doi.org/10.5194/tc-16-4107-2022, 2022.

Jacobs, S., Helmer, H., Doake, C. S. M., Jenkins, A., and Frolich, R. M.: Melting of ice shelves and the mass balance of Antarctica, Journal
    of Glaciology, 38, 375–387, https://doi.org/10.3189/S0022143000002252, 1992.

Jenkins, A.: A one-dimensional model of ice shelf-ocean interaction, Journal of Geophysical Research: Oceans, 96, 20 671–20 677,
    https://doi.org/10.1029/91JC01842, 1991.

345   Jenkins, A.: Convection-driven melting near the grounding lines of ice shelves and tidewater glaciers, Journal of Physical Oceanography, 41, 2279–2294, https://doi.org/10.1175/JPO-D-11-03.1, 2011.

Kobayashi, S., Ota, Y., Harada, Y., Ebita, A., Moriya, M., Onoda, H., Onogi, K., Kamahori, H., Kobayashi, C., Endo, H., Miyaoka, K., and Takahashi, K.: The JRA-55 reanalysis: general specifications and basic characteristics, Journal of the Meteorological Society of Japan. Ser. II, 93, 5–48, https://doi.org/10.2151/jmsj.2015-001, 2015.

350   Kusahara, K. and Hasumi, H.: Modeling Antarctic ice shelf responses to future climate changes and impacts on the ocean, Journal of Geophysical Research: Oceans, 118, 2454–2475, https://doi.org/10.1002/jgrc.20166, 2013.

Kusahara, K., Tatebe, H., Hajima, T., Saito, F., and Kawamiya, M.: Antarctic Sea Ice Holds the Fate of Antarctic Ice-Shelf Basal Melting in a Warming Climate, Journal of Climate, 36, 713 – 743, https://doi.org/10.1175/JCLI-D-22-0079.1, 2023.

Lauber, J., Hattermann, T., de Steur, L., Darelius, E., Auger, M., Nøst, O. A., and Moholdt, G.: Warming beneath an East Antarctic ice shelf
355   due to increased subpolar westerlies and reduced sea ice, Nature Geoscience, 16, 877–885, https://doi.org/10.1038/s41561-023-01273-5, 2023.

Lauber, J., Hattermann, T., de Steur, L., Darelius, E., and Fransson, A.: Hydrography and circulation below Fimbulisen Ice Shelf, East Antarctica, from 12 years of moored observations, EGUsphere, 2024, 1–38, https://doi.org/10.5194/egusphere-2024-904, 2024.

Lindbäck, K., Moholdt, G., Nicholls, K. W., Hattermann, T., Pratap, B., Thamban, M., and Matsuoka, K.: Spatial and temporal varia-
360   tions in basal melting at Nivlisen ice shelf, East Antarctica, derived from phase-sensitive radars, The Cryosphere, 13, 2579–2595, https://doi.org/10.5194/tc-13-2579-2019, 2019.

Morlighem, M.: MEaSUREs BedMachine Antarctica, Version 2. Boulder, Colorado USA. NASA National Snow and Ice Data Center Distributed Active Archive Center, Accessed 12 April 2021, https://doi.org/10.5067/E1QL9HFQ7A8M, 2020.

Morlighem, M., Rignot, E., Binder, T., Blankenship, D., Drews, R., Eagles, G., Eisen, O., Ferraccioli, F., Forsberg, R., Fretwell, P., Goel,
365   V., Greenbaum, J. S., Gudmundsson, H., Guo, J., Helm, V., Hofstede, C., Howat, I., Humbert, A., Jokat, W., Karlsson, N. B., Lee, W. S., Matsuoka, K., Millan, R., Mouginot, J., Paden, J., Pattyn, F., Roberts, J., Rosier, S., Ruppel, A., Seroussi, H., Smith, E. C., Steinhage, D., Sun, B., Broeke, M. R. v. d., Ommen, T. D. v., Wessem, M. v., and Young, D. A.: Deep glacial troughs and stabilizing ridges unveiled beneath the margins of the Antarctic ice sheet, Nature Geoscience, 13, 132–137, https://doi.org/10.1038/s41561-019-0510-8, 2020.

Mouginot, J., Rignot, E., and Scheuchl, B.: MEaSUREs Phase-Based Antarctica Ice Velocity Map, Version 1. Boulder, Colorado USA. NASA
370   National Snow and Ice Data Center Distributed Active Archive Center, Accessed 13 April 2021, https://doi.org/10.5067/PZ3NJ5RXRH10, 2019a.

Mouginot, J., Rignot, E., and Scheuchl, B.: Continent-Wide, Interferometric SAR Phase, Mapping of Antarctic Ice Velocity, Geophysical Research Letters, 46, 9710–9718, https://doi.org/10.1029/2019GL083826, 2019b.

Neckel, N., Drews, R., Rack, W., and Steinhage, D.: Basal melting at the Ekström Ice Shelf, Antarctica, estimated from mass flux divergence,
375   Annals of Glaciology, 53, 294–302, https://doi.org/10.3189/2012AoG60A167, 2012.

Nicholls, K. W.: The study of ice shelf-ocean interaction—techniques and recent results, Advances in Polar Science, 3, 222–230, https://doi.org/10.13679/j.advps.2018.3.00222, 2018.

Nicholls, K. W., Corr, H. F., Stewart, C. L., Lok, L. B., Brennan, P. V., and Vaughan, D. G.: A ground-based radar for mea-
suring vertical strain rates and time-varying basal melt rates in ice sheets and shelves, Journal of Glaciology, 61, 1079–1087,
380   https://doi.org/10.3189/2015JoG15J073, 2015.

Nøst, O. A., Biuw, M., Tverberg, V., Lydersen, C., Hattermann, T., Zhou, Q., Smedsrud, L. H., and Kovacs, K. M.: Eddy overturning of the Antarctic Slope Front controls glacial melting in the Eastern Weddell Sea, Journal of Geophysical Research: Oceans, 116, https://doi.org/10.1029/2011JC006965, 2011.

Pease, C. H.: The size of wind-driven coastal polynyas, Journal of Geophysical Research: Oceans, 92, 7049–7059, https://doi.org/10.1029/JC092iC07p07049, 1987.

Reese, R., Gudmundsson, G. H., Levermann, A., and Winkelmann, R.: The far reach of ice-shelf thinning in Antarctica, Nature Climate Change, 8, 53–57, https://doi.org/10.1038/s41558-017-0020-x, 2018.

Rignot, E., Jacobs, S., Mouginot, J., and Scheuchl, B.: Ice-Shelf Melting Around Antarctica, Science, 341, 266–270, https://doi.org/10.1126/science.1235798, 2013.

Rignot, E., Mouginot, J., Scheuchl, B., van den Broeke, M., van Wessem, M. J., and Morlighem, M.: Four decades of Antarctic Ice Sheet mass balance from 1979 – 2017, Proceedings of the National Academy of Sciences, 116, 1095–1103, https://doi.org/10.1073/pnas.1812883116, 2019.

Shepherd, A., Ivins, E., Rignot, E., Smith, B., van den Broeke, M., Velicogna, I., Whitehouse, P., Briggs, K., Joughin, I., Krinner, G., Nowicki, S., Payne, T., Scambos, T., Schlegel, N., A, G., Agosta, C., Ahlstrøm, A., Babonis, G., Barletta, V., Blazquez, A., Bonin, J., Csatho, B., Cullather, R., Felikson, D., Fettweis, X., Forsberg, R., Gallee, H., Gardner, A., Gilbert, L., Groh, A., Gunter, B., Hanna, E., Harig, C., Helm, V., Horvath, A., Horwath, M., Khan, S., Kjeldsen, K. K., Konrad, H., Langen, P., Lecavalier, B., Loomis, B., Luthcke, S., McMillan, M., Melini, D., Mernild, S., Mohajerani, Y., Moore, P., Mouginot, J., Moyano, G., Muir, A., Nagler, T., Nield, G., Nilsson, J., Noel, B., Otosaka, I., Pattle, M. E., Peltier, W. R., Pie, N., Rietbroek, R., Rott, H., Sandberg-Sørensen, L., Sasgen, I., Save, H., Scheuchl, B., Schrama, E., Schröder, L., Seo, K.-W., Simonsen, S., Slater, T., Spada, G., Sutterley, T., Talpe, M., Tarasov, L., van de Berg, W. J., van der Wal, W., van Wessem, M., Vishwakarma, B. D., Wiese, D., and Wouters, B.: Mass balance of the Antarctic Ice Sheet from 1992 to 2017, Nature, 558, 219–222, https://doi.org/10.1038/s41586-018-0179-y, 2018.

Smith, B. E., Fricker, H. A., Joughin, I. R., and Tulaczyk, S.: An inventory of active subglacial lakes in Antarctica detected by ICESat (2003–2008), Journal of Glaciology, 55, 573–595, https://doi.org/10.3189/002214309789470879, 2009.

Smith, E. C., Hattermann, T., Kuhn, G., Gaedicke, C., Berger, S., Drews, R., Ehlers, T. A., Franke, D., Gromig, R., Hofstede, C., Lambrecht, A., Läufer, A., Mayer, C., Tiedemann, R., Wilhelms, F., and Eisen, O.: Detailed Seismic Bathymetry Beneath Ekström Ice Shelf, Antarctica: Implications for Glacial History and Ice-Ocean Interaction, Geophysical Research Letters, 47, e2019GL086187, https://doi.org/10.1029/2019GL086187, 2020.

Stewart, C. L., Christoffersen, P., Nicholls, K. W., Williams, M. J., and Dowdeswell, J. A.: Basal melting of Ross Ice Shelf from solar heat absorption in an ice-front polynya, Nature Geoscience, 12, 435–440, https://doi.org/10.1038/s41561-019-0356-0, 2019.

Sun, S., Hattermann, T., Pattyn, F., Nicholls, K. W., Drews, R., and Berger, S.: Topographic Shelf Waves Control Seasonal Melting Near Antarctic Ice Shelf Grounding Lines, Geophysical Research Letters, 46, 9824–9832, https://doi.org/10.1029/2019GL083881, 2019.

Thompson, A. F., Stewart, A. L., Spence, P., and Heywood, K. J.: The Antarctic Slope Current in a Changing Climate, Reviews of Geophysics, 56, 741–770, https://doi.org/10.1029/2018RG000624, 2018.

Vernet, M., Geibert, W., Hoppema, M., Brown, P. J., Haas, C., Hellmer, H. H., Jokat, W., Jullion, L., Mazloff, M., Bakker, D. C. E., Brearley, J. A., Croot, P., Hattermann, T., Hauck, J., Hillenbrand, C.-D., Hoppe, C. J. M., Huhn, O., Koch, B. P., Lechtenfeld, O. J., Meredith, M. P., Naveira Garabato, A. C., Nöthig, E.-M., Peeken, I., Rutgers van der Loeff, M. M., Schmidtko, S., Schröder, M., Strass, V. H., Torres-Valdés, S., and Verdy, A.: The Weddell Gyre, Southern Ocean: Present Knowledge and Future Challenges, Reviews of Geophysics, 57, 623–708, https://doi.org/10.1029/2018RG000604, 2019.

Zeising, O. and Humbert, A.: Indication of high basal melting at the EastGRIP drill site on the Northeast Greenland Ice Stream, The
420   Cryosphere, 15, 3119–3128, https://doi.org/10.5194/tc-15-3119-2021, 2021.